1 Improved Prediction of Dimethyl Sulfide (DMS) Distributions in the

2 NE Subarctic Pacific using Machine Learning Algorithms

3 Brandon J. McNabb[1] & Philippe D. Tortell[1,2]

4 [1]Department of Earth, Ocean and Atmospheric Sciences, University of British Columbia, Vancouver, BC V6T 1Z4,
5 Canada
6 [2]Department of Botany, University of British Columbia, Vancouver, BC V6T 1Z4, Canada

7 *Correspondence to*: Brandon J. McNabb (bmcnabb@eoas.ubc.ca)

8   **Abstract.** Dimethyl sulfide (DMS) is a volatile biogenic gas with the potential to influence regional climate as a

9   source of atmospheric aerosols and cloud condensation nuclei (CCN). The complexity of the oceanic DMS cycle

10   presents a challenge in accurately predicting sea-surface concentrations and sea-air fluxes of this gas. In this study,

11   we applied machine learning methods to model the distribution of DMS in the NE Subarctic Pacific (NESAP), a

12   global DMS hot-spot. Using nearly two decades of ship-based DMS observations, combined with satellite-derived

13   oceanographic data, we constructed ensembles of 1000 machine-learning models using two techniques, random

14   forest regression (RFR) and artificial neural networks (ANN). Our models dramatically improve upon existing

15   statistical DMS models, capturing up to 62% of observed DMS variability in the NESAP and demonstrate notable

16   regional patterns that are associated with mesoscale oceanographic variability. In particular, our results indicate a

17   strong coherence between DMS concentrations, sea surface nitrate (SSN) concentrations, photosynthetically active

18   radiation (PAR) and sea surface height anomalies (SSHA), suggesting that NESAP DMS cycling is primarily

19   influenced by heterogenous nutrient availability, light-dependent processes and physical mixing. Based on our

20   model output, we derive summertime, sea-air flux estimates ranging between 0.5-2.0 Tg S yr^{-1} in the NESAP. Our

21   work demonstrates a new approach to capturing spatial and temporal patterns in DMS variability, which is likely

22   applicable to other oceanic regions.

1 Introduction

24   Dimethyl sulfide (DMS), a volatile biogenic gas, is an important component of the marine sulfur cycle.

25   This molecule contributes the largest fraction of bulk non-sea salt (NSS) sulfate emissions to the atmosphere (Bates

26   et al., 1992), where it is rapidly oxidized to form aerosols that act as cloud condensation nuclei (CCN; Charlson et

27   al., 1987; Hegg et al., 1991; Korhonen et al., 2008), potentially influencing regional albedo and climate (Charlson

28   et al., 1987; Ayers and Cainey, 2007). Given its potential role in climate regulation, and recognized importance to

29   marine microbial metabolism (Vila-Costa et al., 2006) and food web interactions (Nevitt, 2008), substantial

30   research has focused on characterizing DMS dynamics in seawater. This work has revealed considerable

31   complexity in the oceanic DMS cycle, which has limited the development of simple predictive algorithms

32   describing spatial and temporal DMS distributions.

33   Oceanic DMS production and loss are tightly linked with the biological cycling of the related metabolites

34   dimethyl sulfoniopropionate (DMSP) and dimethyl sulfoxide (DMSO). DMS is believed to be primarily derived

35   from the cleavage of DMSP (Kiene and Linn, 2000), but it can also be cycled through biological DMSO reduction

36   (Spiese et al., 2009) and oxidation (Lidbury et al., 2016), and abiotically by light-dependent reactions (del Valle et

37   al., 2007; Royer et al., 2016). DMS cycling is influenced by suite of environmental and ecological factors, including

38   release from phytoplankton cells into the dissolved pool via grazing (Dacey and Wakeham, 1986), viral lysis (Malin

39   et al., 1998), or exudation. Oxidative stress generated by other variables such as temperature (Kirst et al., 1991),

40   salinity (Dickson and Kirst, 1987), UV radiation (Kinsey et al., 2016), and nutrient limitation (Bucciarelli et al.,

41   2013; Spiese & Tatarkov, 2014) may also enhance the cycling of DMSP and DMSO, which may regulate DMS

42   concentrations through cascading oxidative pathways (Sunda et al., 2002). Finally, variability in surface wind fields

43   can modulate the rates of DMS sea-air exchange, providing a significant source of heterogeneity in surface water

44   DMS concentrations (Royer et al., 2016). These examples illustrate the complex non-linearity of the oceanic DMS

45   cycle.

46   Over the past two decades, a number of approaches have been developed to model DMS distributions at

47   both global (Bock et al., 2021; Galí et al., 2018; Simó and Dachs, 2002; Vallina and Simó, 2007) and regional (Watanabe

48   et al., 2007) scales. These models have been largely based on linear regression techniques to estimate DMS using

49   one or two predictors. To date, these studies have focused on a number of variables, including ratio of chlorophyll

50   a (Chl-a) to mixed layer depth (MLD) (Simó and Dachs, 2002), sea surface temperature (SST) and nitrate (SSN)

51   (Watanabe et al., 2007), solar radiation dose (SRD) (Vallina and Simó, 2007), photosynthetically active radiation

52   (PAR) and modelled DMSP concentrations (Galí et al., 2018). Some of these models have demonstrated reasonably

53   good performance at global scales, but their predictive power is generally diminished at regional scales (Herr et al.,

54   2019), failing to accurately resolve important smaller-scale features (Belviso et al., 2003; Nemcek et al., 2008;

55   Royer et al., 2015; Tortell, 2005b).

56   In recent years, machine-learning algorithms have been increasingly used to derive predictions for non-

57   linear oceanic systems. For example, these methods have been successfully applied to describe the spatial and

58   temporal patterns of global methane flux (Weber et al., 2019) and carbon export (Roshan and DeVries, 2017). To

59   our knowledge, only two studies have thus far applied machine-learning to describe DMS distributions, with one

60   study focused on the Arctic (Humphries et al., 2012) and the other exploring a global domain (Wang et al., 2020).

61   Despite producing algorithms with reasonable predictive skill, these two studies found limited success in resolving

62   the underlying relationships driving DMS variability. This was partially due to a reliance on indirect sensitivity

63   tests assessing the importance of predictor variables, and also, potentially, from the large-scale averaging applied

64   to the underlying data fields ($1\times1°$; 111 km^2). Analyses at higher spatial resolution may reveal mesoscale (roughly

65   20-200 km) and sub-mesoscale (roughly 1-20 km) patterns that would otherwise be obscured, thereby increasing

66   predictive strength.

67   Machine learning algorithms require large datasets for the training and testing process. Traditionally, DMS
68   measurements were based on time-consuming ship-board analysis of discrete samples, resulting in sparse data
69   coverage over much of the oceans. More recently, the development of several automated DMS measurement
70   systems (Royer et al., 2014; Saltzman et al., 2009; Tortell, 2005a) has provided marine DMS observations at a
71   significantly higher resolution, yielding greater spatial and temporal data coverage. These new datasets potentially
72   enable new insights into small-scale and regional patterns in oceanic DMS distributions, as well as the
73   characterization of oceanic DMS 'hot-spots'. One such global DMS hotspot is the northeast subarctic Pacific
74   (NESAP) (Asher et al., 2017; Herr et al., 2019; Lana et al., 2011), a region encompassing both highly productive
75   coastal upwelling regimes, and off-shore, iron-limited waters (Martin and Fitzwater, 1988). Several factors have
76   been proposed to account for the elevated DMS production in the NESAP, including increased productivity from
77   entrainment and upwelling along coastal fronts (Asher et al., 2017), and the stimulation of DMS production in
78   response to oxidative stress in low iron waters (Sunda et al., 2002; Herr et al., 2020). Although multiple studies
79   have examined empirical relationships between DMS and various oceanographic factors in the NESAP (Watanabe
80   et al., 2007; Herr et al., 2019; Asher et al., 2017, 2011), these have all reported low predictive skill based on simple
81   linear correlation approaches. To date, machine-learning approaches have not been applied to describe DMS
82   distributions specifically in this region.

83   Here, we present an approach to modelling summertime NESAP DMS concentrations and sea-air fluxes
84   using ensemble random forest regression (RFR) and artificial neural network (ANN) machine-learning algorithms.
85   Our statistical models leverage field observations of DMS collected across the NESAP between 1997 to 2017 to
86   generate a summertime DMS climatology mapped at a higher spatial resolution than previous efforts (Simó and
87   Dachs, 2002; Vallina and Simó, 2007; Galí et al., 2018; Watanabe et al., 2007; Humphries et al., 2012; Wang et
88   al., 2020). This new modelling approach represents a significant improvement over previous methods and predicts
89   regional DMS distributions that are coherent with underlying patterns of oceanographic variability. Most notably,
90   the modelled DMS concentrations and sea-air fluxes can be explained, to a large extent, by regional and mesoscale
91   patterns in nutrient supply and physical mixing dynamics. Based on the output of our models, we present
92   summertime sea-air flux estimates in close agreement with previous studies (Herr et al., 2019; Lana et al., 2011),
93   further highlighting the importance of the NESAP as a globally-significant sulfur source to the atmosphere.

2 Methods

2.1 Data

A combination of data sources was used in training our machine-learning models to build a summertime DMS climatology. For this study, we restricted DMS measurements to the months of June, July and August between 1997 to 2017 in the NESAP (43-60ºN, 147-122ºW). A total of 26,201 data points were obtained from the NOAA PMEL repository (https://saga.pmel.noaa.gov/dms/; last accessed: February 3, 2021), including measurements derived from purge and trap gas chromatography and membrane inlet mass spectrometry. The DMS data were binned to a monthly resolution, regardless of year, and averaged into 0.25 x 0.25º grid cells.

Predictor data used to build our machine-learning models included the following variables derived from the NASA Aqua MODIS satellite at level L3 monthly 0.036º resolution: sea surface temperature (SST), the ratio of normalized fluorescence line height to chlorophyll a (nFLH:Chl-a), instantaneous and daily observed photosynthetically active radiation (iPAR and PAR, respectively), particulate inorganic carbon (PIC), the absorption of gelbstof and detritus at 433 nm (a_{cdm}(443)), and diffuse attenuation coefficients at 490nm (K_d). Satellite-based PIC is considered as a proxy for the abundance of coccolithophores and other calcified phytoplankton (Franklin et al., 2010), whereas the a_{cdm}(443) product is considered a proxy for the distributions of chromophoric dissolved organic matter (CDOM) (Nelson & Siegel, 2013), which is thought to be an important photosensitizer of DMS (see Sect. 4.1). For observations prior to 2004, data were from either SeaWiFS or Terra MODIS when SeaWiFS data was unavailable (*e.g.* nFLH and iPAR). As described below, K_d and PIC were later excluded from the final models (see Sect. 2.6).

The following predictor variables were also used: 6-day averaged sea surface height anomalies (SSHA) derived from the TOPEX/Poseidon satellites at 0.17º resolution; Level L4 ESA Sentinal-3 Copernicus monthly-averaged 0.25º wind speeds; net primary productivity (NPP) from the Vertically-Generalized Production Model (VGPM; Behrenfeld & Falkowski, 1997) at monthly 0.25º resolution; sea surface nitrate from the 2018 World Ocean Atlas at monthly 1º resolution (Garcia et al., 2019); and mixed-layer depth (MLD) and sea surface salinity (SSS) from the MIMOC climatology at 0.5º resolution (Schmidtko et al., 2013). Except for MIMOC data, all predictors were restricted in time to the corresponding years of DMS sampling (1997 to 2017). Net community productivity (NCP) was estimated from the algorithm of Li & Cassar, (2016; using NPP and SST). As with DMS observations, predictor data were interpolated to a 0.25 x 0.25º average monthly resolution using linear radial basis interpolation functions. Interpolation was constrained to the oceanic region by masking out land pixels using ETOPO2 bathymetric (0.033º resolution) binned at 0.25 x 0.25º resolution. Data sources can be found in Table 1.

124

Table 1. Data sources and spatial and temporal resolution of predictor variables used to develop the RFR and ANN algorithms. Data processing levels are indicated where relevant. All variables were used as predictors (excluding bathymetry) and post-processed to monthly-averaged, 0.25º resolution (see sections 2.1-2.2).

Variable	Spatial Resolution (º)	Temporal Resolution	Source	Level
Sea Surface Temperature (SST)	0.036	6-Day Average	SeaWiFS/AquaTERRA (1997-2003) or AquaMODIS(2004-2017): https://oceancolor.gsfc.nasa.gov/l3/	3
Chlorophyll-Normalized Fluorescence (nFLH:Chl-a)	0.036	Monthly	SeaWiFS/AquaTERRA (1997-2003) or AquaMODIS (2004-2017): https://oceancolor.gsfc.nasa.gov/l3/	3
Instantaneous Photosynthetically Active Radiation (iPAR)	0.036	Monthly	SeaWiFS/AquaTERRA (1997-2003) or AquaMODIS (2004-2017): https://oceancolor.gsfc.nasa.gov/l3/	3
Daily Photosynthetically Active Radiation (PAR)	0.036	Monthly	SeaWiFS/AquaTERRA (1997-2003) or AquaMODIS (2004-2017): https://oceancolor.gsfc.nasa.gov/l3/	3
Particulate Inorganic Carbon (Calcite; PIC)	0.036	Monthly	SeaWiFS/AquaTERRA (1997-2003) or AquaMODIS (2004-2017): https://oceancolor.gsfc.nasa.gov/l3/	3
Absorbtion of Gelbstof and Detritus at 433 nm ($a_{cdm}(443)$)	0.036	Monthly	SeaWiFS/AquaTERRA (1997-2003) or AquaMODIS (2004-2017): https://oceancolor.gsfc.nasa.gov/l3/	3
Diffuse Attenuation Coeffiencents at 490 nm (K_d)	0.036	Monthly	SeaWiFS/AquaTERRA (1997-2003) or AquaMODIS (2004-2017): https://oceancolor.gsfc.nasa.gov/l3/	3
Sea Surface Height Anomalies (SSHA)	0.17	Monthly	TOPEX/Poseidon: https://podaac.jpl.nasa.gov/dataset/SEA_SURFACE_HEIGHT_ALT_GRIDS_L4_2SATS_5DAY_6THDEG_V_JPL1812	4
Monthly Wind Speeds	0.25	Monthly	ESA Sentinal-3 Copernicus: https://resources.marine.copernicus.eu/?option=com_csw&view=details&product_id=WIND_GLO_PHY_CLIMATE_L4_REP_012_003	N/A

Net Primary Productivity (NPP)	0.25	Monthly	Vertically-Generalized Production Model (VGPM): http://www.science.oregonstate.edu/ocean.productivity/	N/A
Sea Surface Nitrate (SSN)	1	Monthly	World Ocean Atlas 2018 (WO18): https://www.ncei.noaa.gov/access/world-ocean-atlas-2018/	N/A
Mixed Layer Depth (MLD)	0.5	Monthly	MIMOC Climatology: https://www.pmel.noaa.gov/mimoc/	N/A
Sea Surface Salinity (SSS)	0.5	Monthly	MIMOC Climatology: https://www.pmel.noaa.gov/mimoc/	N/A
Bathymetry	0.033	N/A	ETOPO2: https://rda.ucar.edu/datasets/ds759.3/	N/A

128

129

2.2 Machine-learning models

131   We compared the performance of random forest regression (RFR) and artificial neural network (ANN)
132   models at the regional scale. In both cases, the models were built as an ensemble of either 1000 individual decision
133   trees or individual networks to minimize bias in predictions. The input data were randomly divided for use in model
134   training (80%) and external testing (20%). Although RFR is not sensitive to large differences in predictor variance,
135   predictor data were standardized in both models by normalization to their respective mean and standard deviation.
136   Additionally, we applied an inverse hyperbolic sine (IHS) transformation to the DMS data prior to training. Testing
137   results indicated that IHS yielded slightly better performance than the more traditional logarithmic transformations
138   for both of our models.

139   Both our ANN and RFR models followed a similar design to Weber et al. (2019). Our ANNs were built
140   using a feed-forward framework consisting of a single input node, two hidden layers each consisting of 30 neurons
141   (using a sigmoidal activation function), and a single output layer (using a linear activation function). A Bayesian
142   L2 (Ridge) regularization parameter was tuned to minimize overfitting. Each individual decision tree within the
143   RFR was trained using the standard CART algorithm and constrained to a max depth of 25 decision splits, the
144   simplest configuration determined to perform well and minimize overfitting.

2.3 Sea-to-air fluxes

146   Sea-air DMS fluxes (F_{DMS}, µmol m^{-2} d^{-1}) were calculated from the monthly-averaged observed and
147   modelled DMS values for June, July and August. F_{DMS} was calculated using the gas transfer velocity (k, cm^3 hr^{-1})
148   following the modified approach of Webb et al. (2019):

149    $$F_{DMS} = k(DMS)(0.24) \tag{1}$$

150   where the factor of 0.24 converts to the values to daily fluxes. Since our fluxes were calculated from our monthly
151   averaged models, the gas transfer velocity was calculated using the approach from Simó & Dachs (2002), as
152   modified by (Nightingale et al., 2000). This approach is necessary to correct for differences due to the non-linear
153   relationship between DMS and wind speed (Livingstone and Imboden, 1993) when using monthly-averaged,
154   satellite-derived wind speeds. Assuming a Rayleigh distribution (ξ =2), k can be defined as:

155    $$k = [5.88\eta\Gamma(1 + \frac{2}{\xi}) + 1.49\eta\Gamma(s)]Sc_{DMS}^{-0.5} \tag{2}$$

156   where η is the quotient of the wind speed (m s⁻¹) by the gamma function $\Gamma(s)$ (using $s = 1 + \frac{1}{\xi}$), and Sc_{DMS} is the

157   DMS-specific Schmidt number (cm³ hr⁻¹) as defined by Saltzman et al. (1993):

158   $Sc_{DMS} = 2674 - 147.12(SST) + 3.72(SST^2) - 0.038(SST^3)$ (3)

159   Regional summertime fluxes ($\overline{F}_{DMS}$, Tg) were calculated as the average quantity of DMS-sulfur emitted

160   over 92 days through the area of the mapped study region (1.28x10⁷ km² or 85.0% of the total bounded area).

2.4 Comparison against existing algorithms

162   Simple linear regression (LR) and multiple linear regression (MLR) models were built for comparison

163   against the machine-learning algorithms. We also tested the performance of our RFR and ANN models against the

164   published algorithms of Simó & Dachs (2002), Watanabe et al. (2007), Vallina & Simó, (2007), and Galí et al.

165   (2018) (hereafter referred to as SD02, W07, VS07, and G18, respectively). SRD is calculated here using MLD as

166   described by Vallina & Simó (2007):

167   $SRD = \frac{PAR}{K_d \times MLD} \times (1 - e^{-K_d \times MLD})$ (4)

168   Each of the four algorithms was assessed using both their original coefficients and coefficients tuned to

169   our NESAP dataset using nonlinear least-squares optimization.

2.5 Controls on DMS variability

171   Principal component analysis (PCA) was applied to assess the relationships between DMS and the nine

172   predictors used to build the RFR and ANN ensembles. Additionally, non-parametric spearman rank correlations

173   were calculated between each variable and both the modelled and observed DMS concentrations. Correlation

174   analysis was also extended to assess the role of taxonomy on predicted DMS concentrations, using the outputs of

175   a chlorophyll-a based taxonomic algorithm by Hirata et al. (2011) with NESAP-tuned coefficients (Zeng et al.,

176   2018).

2.6 Sensitivity Tests and Predictor Selection

178   To inform our selection of grid size, we assessed the performance of both the RFR and ANN models using

179   grid cells ranging from 0.25 to 5° (Fig. 1). From this analysis, we found that model accuracy was highest at 0.25°

180   resolution (see Sect. 3.1). Smaller grid sizes would presumably further improve model accuracy, but at a

181   significantly higher computational cost.

182   We also tested the influence of other biological predictor variables on the performance of the RFR and

183   ANN models, using either NCP, NPP, Chl-a, or PIC. These sensitivity tests indicated no significant difference

184   between the various biological predictor variables, although accuracy was slightly reduced when PIC was used.

185   We therefore selected NCP as the biological predictor variable within our model framework. We also removed K_d

186   as a predictor variable after further sensitivity testing indicated that its exclusion slightly improved results.

187   The inclusion of nFLH:Chl-a represents a proxy for iron limitation (see Sect. 4.1). However, fluorescence

188   yields corrected for non-photochemical quenching (NPQ) have been suggested to yield a better iron limitation

189   proxy than nFLH:Chl-a (Behrenfeld et al., 2009). We therefore calculated NPQ-corrected fluorescence yields (φ_f)

190   by:

191     $$\varphi_f = \frac{nFLH}{Chl-a \times \alpha \times S} \times \frac{iPAR}{iPAR} \qquad (5)$$

192   where $\alpha = 0.0147 \times Chl - a^{-0.316}$ and $S = 100 \text{ mW cm}^{-2} \text{ μm}^{-1} \text{ sr}^1 \text{ m}$ as described by Behrenfeld et al. (2009). Our

193   tests indicated nFLH:Chl-a yielded slightly improved performance overall whereas φ_f decreased both models'

194   performance. We therefore retained nFLH:Chl-a and excluded φ_f in our final model design.
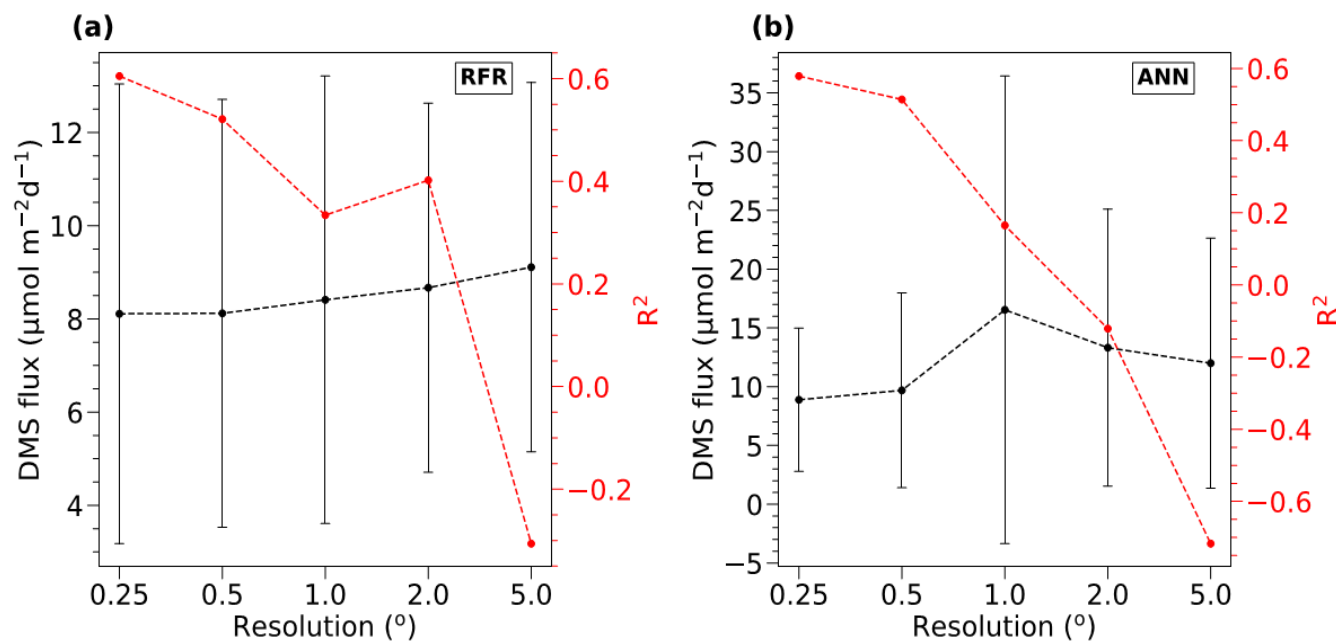
195

196   **Fig. 1. Sensitivity of RFR and ANN models to grid size resolution. DMS fluxes (green) and R2 values (red) derived from sensitivity**

197   **tests of (a) RFR and (b) ANN models to pixels resolutions of 0.25-5°. The negative R2 values observed at the lowest resolution (largest**

198   **grid cells) indicate that the predicted values explain less variance than the overall mean of the dataset.**

3 Results

3.1 Model evaluation

To benchmark the performance of our RFR and ANN models, we first evaluated the predictive skill of four existing empirical DMS algorithms (SD02, W07, VS07, & G18), in addition to simple and multiple linear regression models. Previous studies have demonstrated that these empirical algorithms show strong predictive skill (R^2=0.53-0.84) over large scales and in some oceanic regions (Simó and Dachs, 2002; Galí et al., 2018; Watanabe et al., 2007), but significantly poorer performance in the NESAP (Herr et al., 2019). Consistent with these results, we found that the SD02, W07, VS07, and G18 did not accurately predict NESAP DMS distributions, even with regionally tuned coefficients (Fig. 2, R^2=0-0.01). We also found that simple and multiple linear regressions performed poorly (R^2=0-0.05; Fig. 2, 3), yielding virtually no explanatory power for surface water DMS distributions in the NESAP ($R^2 \leq 0.05$).

210
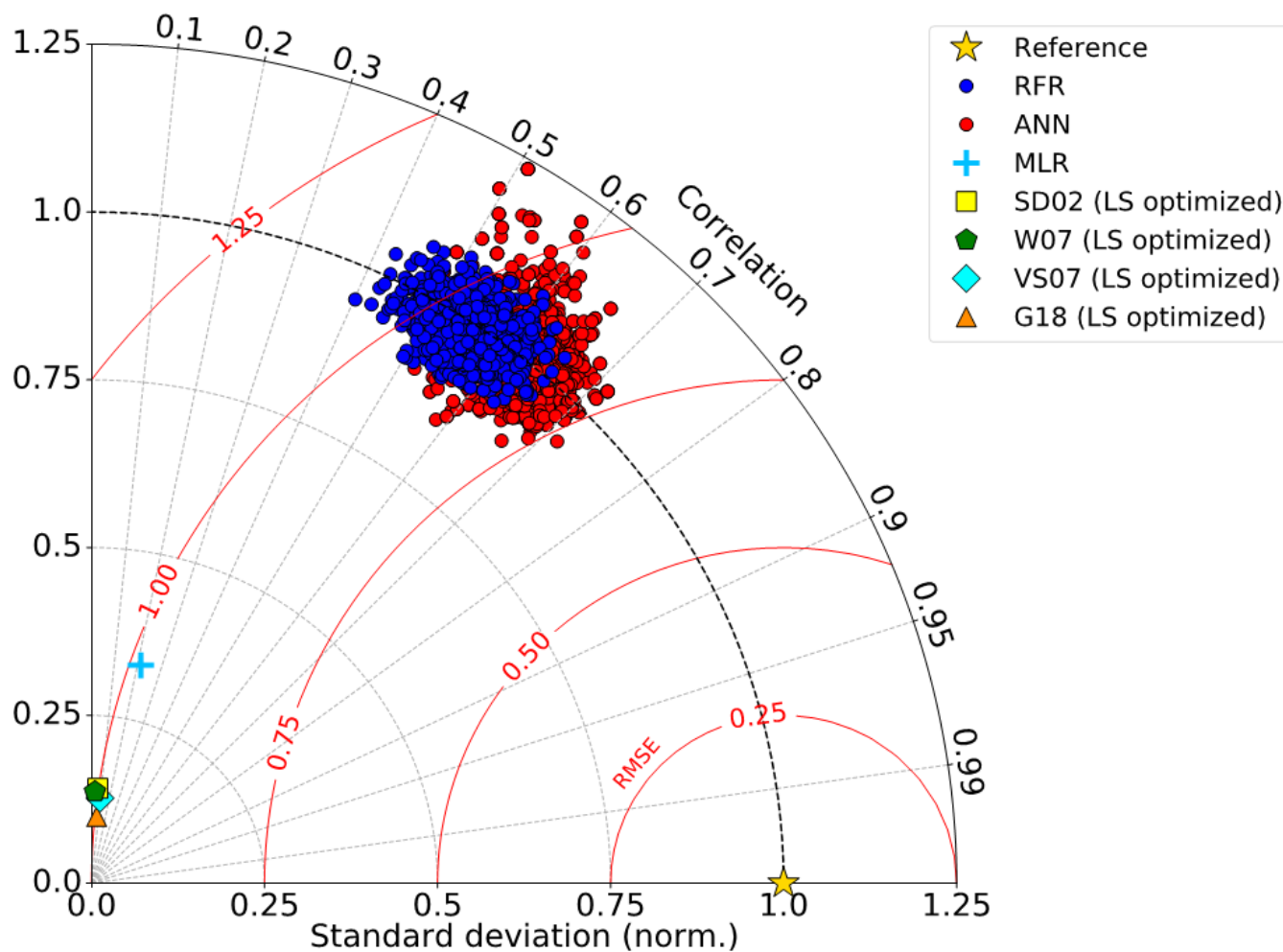
Fig. 2. Taylor Diagram showing comparative performance metrics of each individual Random Forest Regression (RFR) and Artificial Neural Network (ANN) model (1000-model ensembles) against multiple linear regression (MLR) and other statistical DMS models (See sections 2.1 and 2.4). The Pearson correlation coefficients ("Correlation"; outer radius), root mean squared error ("RMSE"; red radial contours), and standard deviations (SDs; grey radial contours from origin) are all computed with respect to the observed DMS samples after inverse hyperbolic sine (IHS) transformation. The reference of a perfect model fit is shown with a gold star. SDs of the model outputs are normalized to the SDs of the DMS observations. RMSE represents a normalized trigonometric derivation from both the correlation coefficients and normalized SDs. Performance of the SDO2, W07, VS07, and G18 algorithms reported here are calculated using regionally tuned coefficients to the NESAP derived from non-linear least-squares optimization (see section 2.4).

221   Relative to other published modelling approaches, both the RFR and ANN models dramatically improved

222   the representation of NESAP DMS variability, achieving significantly higher predictive accuracy (Fig. 2, 3). The

223   collective ensembles of both the RFR and ANN models yielded strong performance, explaining up to 62% of the

224   observed DMS variability (R^2=0.61-0.62; Fig. 3). For individual models within the ensembles, the AAN method

225 provided slightly better results (R^2=0.16-0.50), compared to the individual RFR models (R^2=0.16-0.43). As

226 observed for predicted DMS concentrations, the models showed lower predictive power for sea-air DMS fluxes at

227 coarser resolution (Fig. 1).

228
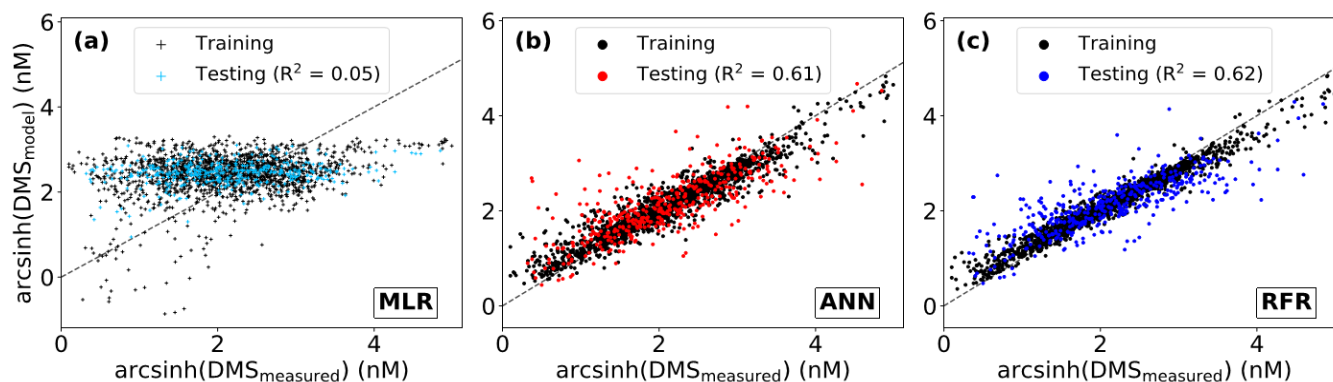
229 **Fig. 3. Performance of three modelling approaches in predicting observed DMS distributions; (A) multiple linear**
230 **regression (MLR) (B) ensemble of Artificial Neural Networks (ANN) and (C) ensemble of Random Forest Regression**
231 **(RFR). For consistency, all predictions are partitioned by the Training and Testing datasets used to build the ensembles**
232 **(see section 2.2). Model performance (R^2) is computed only for the Testing dataset predictions. The dashed line**
233 **demonstrates a 1:1 relationship.**

234 **3.2 DMS distributions and sea-air fluxes**

235   The predicted spatial distribution of DMS was generally consistent between observations and the RFR and

236 ANN methods (Fig. 4a,c,d). The average model derived DMS concentrations was 4.0 ± 2.1 nM and 4.7 ± 3.0 nM

237 (mean ± SD) for the RFR and ANN ensemble models, respectively, with a similar range from 0.3 to 84.3 nM. In

238 both models, the highest DMS concentrations were largely constrained to coastlines and within the Alaska Gyre

239 adjacent to the Aleutian Islands (Fig. 4b-c, 8C). The greatest discrepancy between DMS concentrations from the

240 two models was observed in these regional 'hotspots', where the ANN models emphasize high DMS within the

241 Alaska gyre, while the RFR models emphasize elevated coastal DMS concentrations (Fig. 4b). The models deviated

242 on average by 0.49 nM, with the greatest offsets observed in an area of particularly sparse DMS observations in

243 the Alaska Gyre (Fig. 4a,b). Future observational data in this region should help improve model performance.

244

June – August
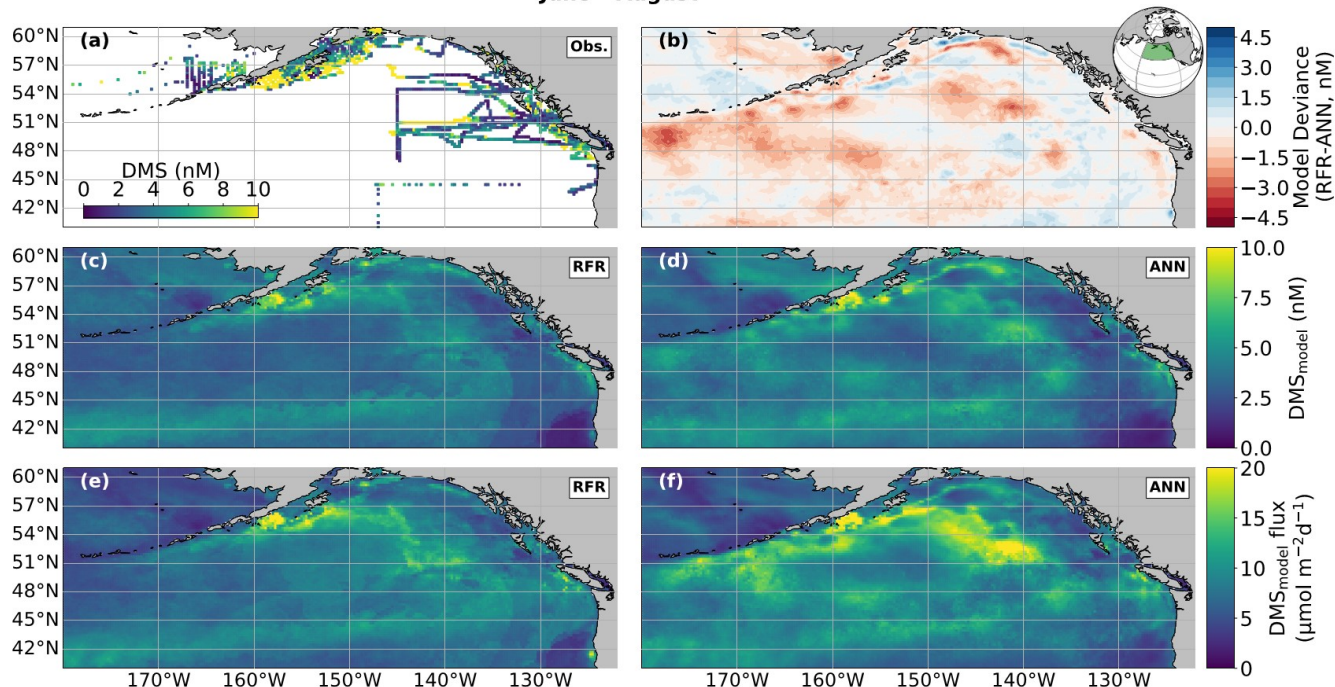
Fig. 4. **Predicted maps of sea surface DMS concentrations and sea-air fluxes. (a) Ship-based observations of mean summertime (June-August) DMS concentrations used to construct the predictive models. (b) Differences between the (c) Random Forest Regression (RFR) and (d) Artificial Neural Network (ANN) ensemble predicted DMS concentrations. (e,f) DMS sea-air fluxes derived from the predicted DMS concentrations. Colormap ranges are restricted to illustrate trends, with <1% of DMS data exceeding the colorbar limits. The inset map in (b) shows the NESAP study region as a shaded green patch in a global orthographic projection.**

Sea-air DMS fluxes (Fig. 4e,f) derived from ANN predictions were 18% higher, on average, than RFR predictions, largely due to higher predicted values in the Alaska Gyre (Fig. 4d-e, Table 2). The distribution of ANN sea-air fluxes was also closer to ship-based observations (Fig. 5). Predicted regional fluxes ranged from 0.7 to 107 μmol m^{-2} d^{-1} between the two models (Fig. 4e,f, 5), with the highest predicted DMS emissions in August, when derived sea-air fluxes were approximately 1.5-fold greater than in June and July (Table 2). Our models yielded a summertime integrated sea-air flux of 0.31±0.19 Tg DMS-derived sulfur (equivalent to 0.5 to 2.0 Tg S yr^{-1}; Table 2), in good agreement with recent estimates based on compiled ship-based observations (0.3 Tg; Herr et al., 2019) and existing climatological estimates (Table 2; Lana et al., 2011). This summertime mean value is equivalent to ~4-8% of total global DMS sea-air emissions annually, assuming an uncertainty ranging between 15 to 28 Tg S yr^{-1} in global estimates (Bock et al., 2021). This result further emphasizes the NESAP as a globally significant DMS source to the atmosphere.

264 **Table 2. Monthly and mean summertime NESAP sea-air DMS fluxes. Fluxes (mean ± SD) are calculated from the**
265 **Random Forest Regression (RFR) and Artificial Neural Network (ANN) model predictions (based on an ensemble of**
266 **2000 models). NESAP sea-air flux derived from the Lana et al. (2011) climatology is shown for comparative purposes.**

267

	RFR	ANN	Annual Sulfur Emissions	
			This Study	Lana et al. (2011)
	$\mu mol\ m^{-2}\ d^{-1}$	$\mu mol\ m^{-2}\ d^{-1}$	Tg S	Tg S
June	5.9 ± 3.7	6.0 ± 3.9	0.22 ± 0.13	0.44 ± 0.20
July	6.5 ± 3.0	7.7 ± 3.8	0.26 ± 0.12	0.33 ± 0.17
August	10.8 ± 3.0	14.0 ± 3.8	0.45 ± 0.21	0.54 ± 0.21
June-August	7.7 ± 2.4	9.2 ± 3.4	0.31 ± 0.19	0.44 ± 0.21

268
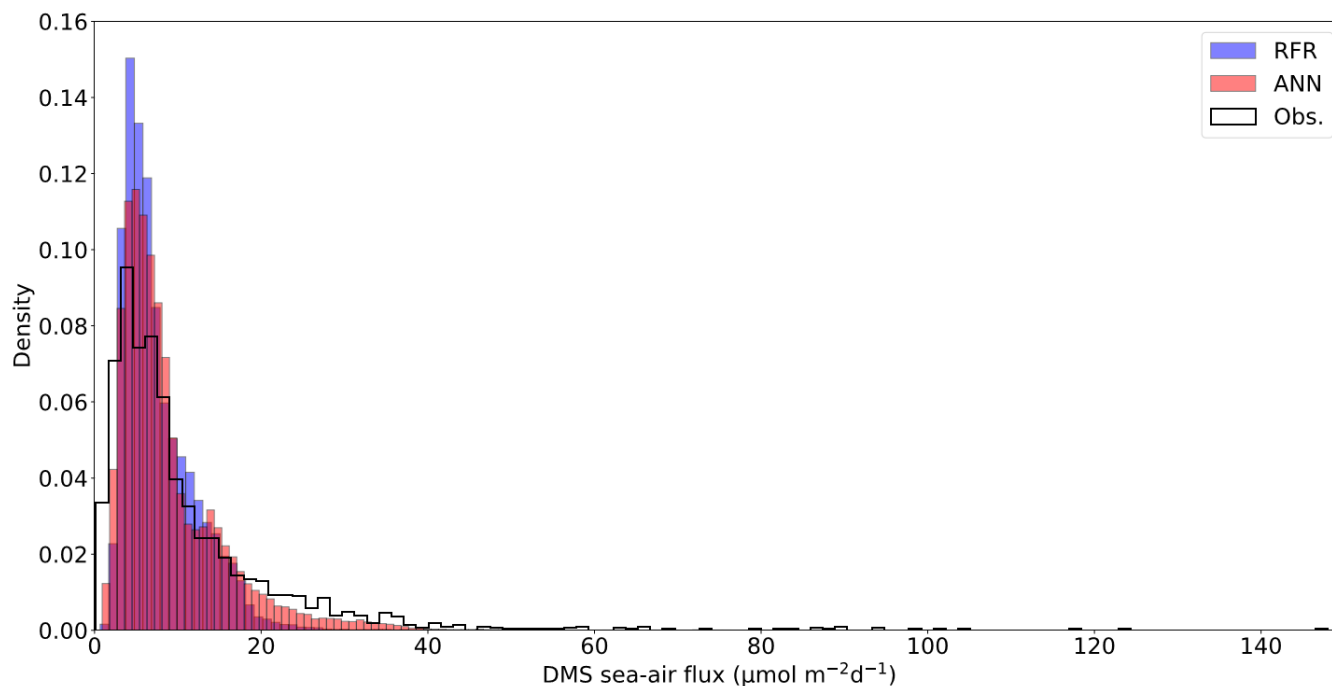
269

270 **Fig. 5. Histograms of DMS sea-air flux distributions derived from the 1000-model ensemble random forest regression (RFR) and**
271 **artificial neural network (ANN) predictions as well as cruise observations (Obs.). The sample sizes of both models are equivalent**
272 **(n= 49,632) and are significantly higher than the observational dataset (n=2063). Note that the ANN better predicts the upper tail of**
273 **DMS observations greater than 20 nM.**

274

3.4 Drivers of DMS variability

In addition to modelling the spatial and temporal distribution of surface water DMS in the NESAP, we examined the influence of different oceanographic variables as model predictors. As expected based on previous work (Herr et al., 2019), no single predictor was found to exert a dominant control on modelled DMS distributions from either the RFR or ANN models (Fig. 6, 7). Rather, the relationship between DMS and other oceanographic variables exhibited significant region-specific patterns. One of the most compelling regional signatures was the apparent relationship between DMS and SSHA. In both models, we found significant positive correlations between DMS and SSHA (ρ=0.35, 0.41 for RFR and ANN, respectively) across the full spatial domain, with a particularly notable relationship along the northern Alaskan coastline (Fig. 8, 9). Here, strong winds (Fig. 9j-l), coupled with the northeastern Alaska current flow, produce two characteristic oceanographic features in the NESAP: strong, semi-permanent mesoscale eddies collectively referred to as the Haida, Sitka and Yakutat eddies (Fig. 8a), and the formation of the high nutrient, low chlorophyll (HNLC) Alaska Gyre (Fig. 8c; Okkonen et al., 2001; Whitney et al., 2005). Both the monthly (Fig. 9a-i) and summertime-averaged (Fig. 8a,b) RFR and ANN-derived DMS concentrations are low where these downwelling eddies form. In contrast, elevated DMS concentrations were associated with the negative SSHA coastal upwelling areas (Fig. 8a,b), where phytoplankton productivity is stimulated by nutrient inputs into the mixed layer.

291

292
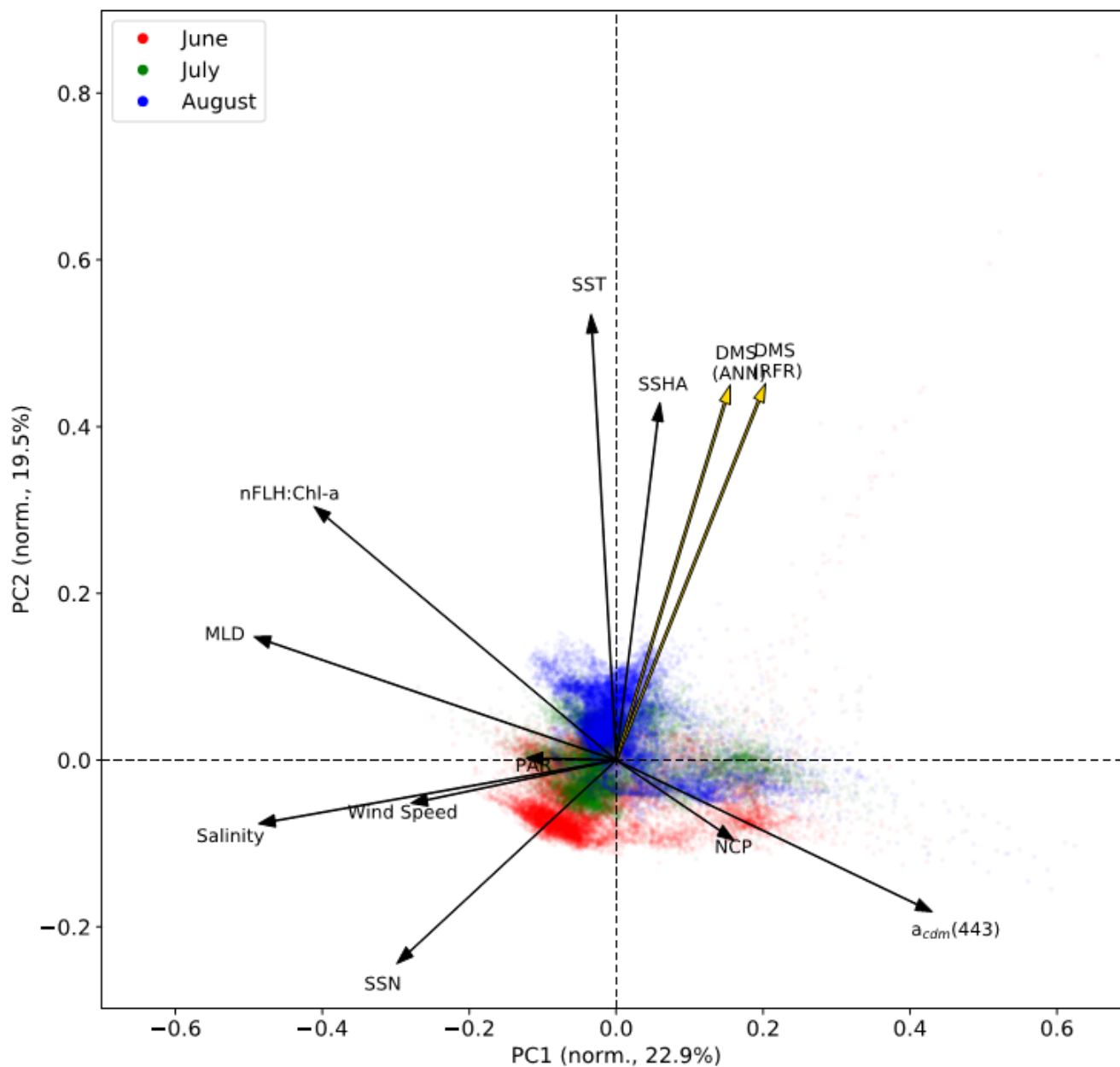
Fig. 6. Principal Component Analysis (PCA) showing the relationships between variables used to construct the predictive algorithms. Eigenvectors (arrows) are superimposed over the principal components (PCs; data points) for the first two significant modes obtained from PCA. PCs are normalized and clustered by month (June-August, see legend for colors), while the eigenvectors are grouped by ensemble model predictions (gold) and nine predictor variables (black). The percentage of variance explained by each mode is indicated along the axes.

298
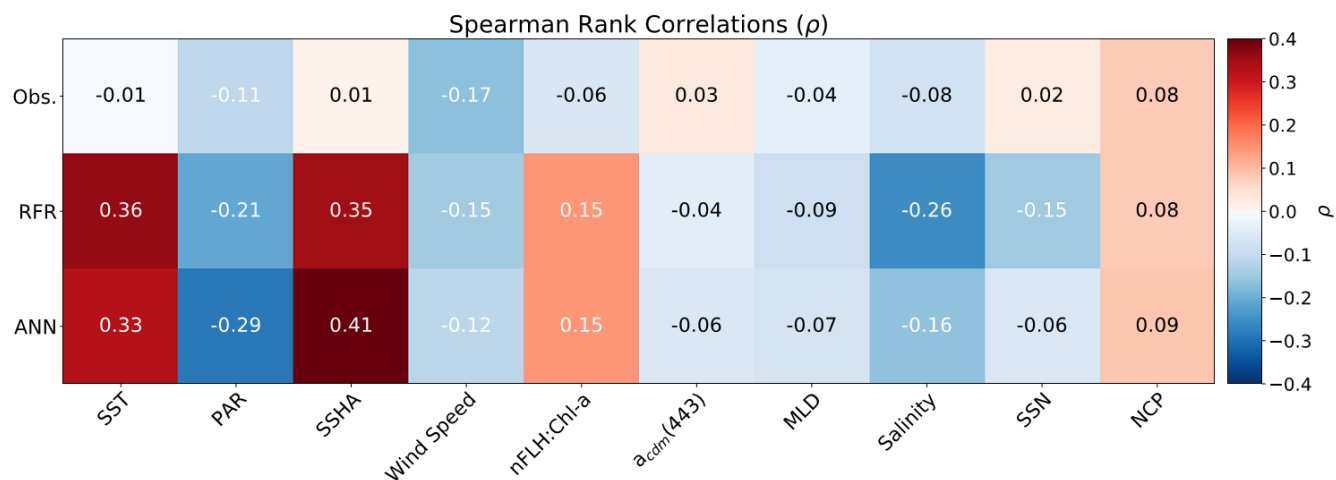
Fig. 7. Heatmap of Spearman rank correlations (ρ). Top row: observed DMS concentrations; middle row: RFR model predictions; bottom row: ANN model predictions. All model correlations are computed on the 1000-model ensembles.

Modelled DMS concentrations also significantly correlated with hydrographic frontal patterns. We found significant correlations between DMS and SST (ρ=0.36, 0.33 for RFR and ANN, respectively) which suggested the central Alaska Gyre is an area of elevated DMS variability. Both models predict high DMS levels in the northern frontal zone of the gyre (140°W-145°W) between the 10.5 and 12°C isotherms and the southern frontal zone between (42°N-45°N) between the 13.5 and 15°C isotherms (Fig. 8b,c). By comparison, our models suggest that DMS concentrations are predominantly low in relation to high sea surface nitrate (SSN) concentrations within the HNLC gyre (Fig. 8, 9). As discussed below, the relationship between DMS and macronutrient concentrations in the HNLC waters of the central Gulf of Alaska could indicate an important role for iron limitation as a controlling factor in the DMS cycle. The presence of elevated summer nutrients in offshore waters is taken as a proxy for iron limitation, which increases over the course of the summer growing season.
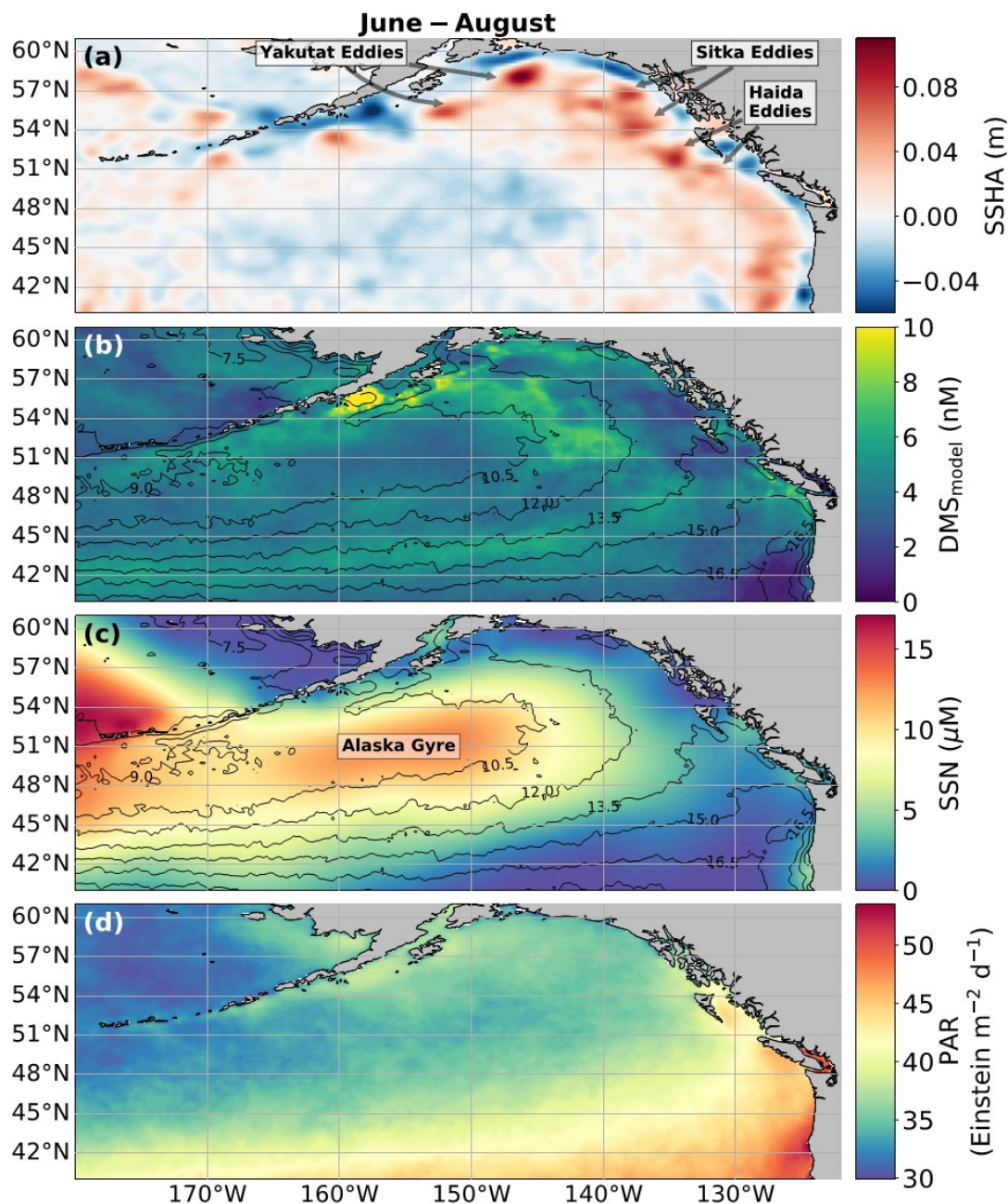
Fig. 8. Physical drivers of summertime (June-August) NESAP DMS distributions. (a) Sea surface height anomalies (SSHA), (b) predicted DMS concentrations derived from the mean of all 2000 RFR and ANN machine learning models, (c) sea surface nitrate (SSN) and (d) photosynthetically active radiation (PAR). Contours in (b,c) show sea surface temperature (SST) isotherms. Coherent features of elevated sea-surface height indicate the presence of mesoscale eddies, whereas nearshore low SSHAs features reveal areas of upwelling. Colormaps ranges are restricted to illustrate trends with <1% of data exceeding the colorbar limits.

318   Other variables appear to exhibit a more localized or minimal influence on DMS cycling. For instance,
319   both NCP and DMS are elevated in productive nearshore waters, but NCP generally correlates weakly with both
320   RFR- and ANN-derived DMS concentrations (ρ=0.08, 0.09 for RFR and ANN, respectively). Similarly, modelled
321   phytoplankton taxonomic composition (Hirata et al., 2011; Zeng et al., 2018) was not significantly correlated with
322   predicted DMS concentrations (ρ<0.1). Although strong, persistent winds appear to sustain low DMS
323   concentrations off the coast of Oregon and Vancouver Island (Fig. 9), wind speeds only weakly correlate with DMS
324   overall for the region (ρ=-0.15 and -0.12 for RFR and ANN, respectively). Additionally, high PAR in these areas
325   correspond with low DMS concentrations (Fig. 6d) and there is an overall negative correlation between PAR and
326   DMS for the region (Fig. 6, 7; ρ=-0.21 and -0.29 for RFR and ANN, respectively). Finally, despite hypothesized
327   links between DMS cycling and iron limitation in the NESAP (Levasseur et al., 2006; Merzouk et al., 2006),
328   nFLH:Chl-a ratios (taken as a proxy for phytoplankton iron stress; Behrenfeld et al., 2009; Westberry et al., 2013)
329   did not exhibit any coherent spatial patterns and only weakly correlated to our modelled DMS concentrations
330   (ρ=0.15 for both RFR and ANN, respectively).
331
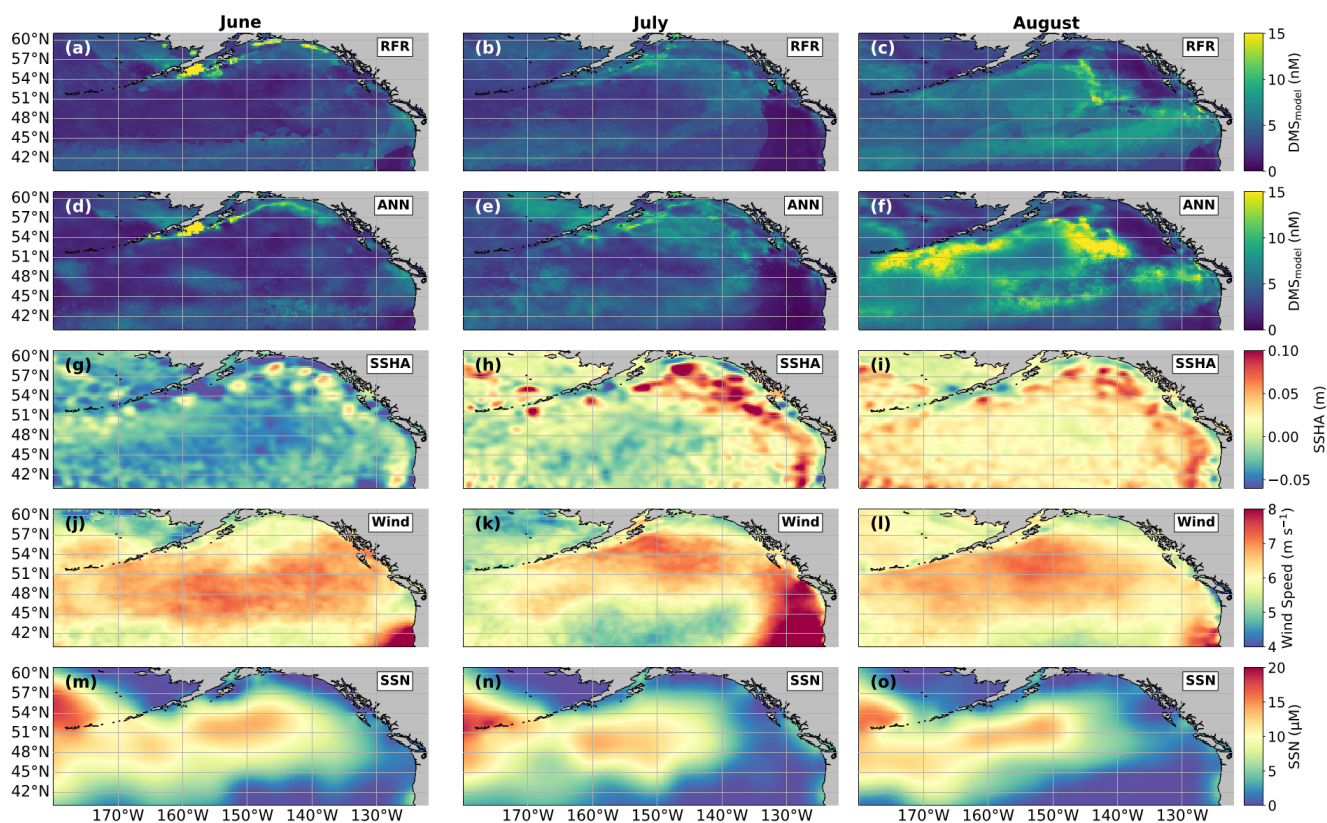
Fig. 9. Predicted spatial and temporal (June-August) DMS distribution in relation to underlying oceanographic variables. DMS concentrations predicted from (a-c) the Random Forest Regression (RFR) and (d-f) the Artificial Neural Network (ANN) ensemble models are mapped alongside the monthly-averaged (g-i) sea surface height anomalies (SSHA), (j-l) wind speeds (Wind), and (m-o) sea surface nitrate (SSN) for each month. Colormap ranges are restricted to illustrate trends, with at most 1.5% of the data beyond the colorbar limits.

4 Discussion

The relative sparsity of DMS data in many oceanic regions and the complexity of DMS cycling have limited previous attempts to model oceanic distributions of this compound (Simó and Dachs, 2002; Vallina and Simó, 2007; Galí et al., 2018; Watanabe et al., 2007; Herr et al., 2019). Taking advantage of expanding data resources, we employed a new approach to statistically describe DMS distributions in the NESAP. Our results show that both our RFR and ANN models substantially improved predictive strength over traditional empirical approaches (Fig. 2, 3), while identifying several key DMS relationships and regional patterns across the NESAP (Fig. 8, 9). Although our statistical approach does not directly elucidate the underlying mechanisms driving these relationships, we can

346 nonetheless make some reasonable inductive inferences. These inferences are discussed below, along with the
347 implications of the improved predictive performance observed here.

4.1 Relationships with other oceanographic variables

349   Among the more prominent spatial relationships we observed was the coherence between predicted DMS
350 concentrations and SST, and the negative correlation between predicted DMS concentrations and sea surface nitrate
351 (SSN) within and surrounding the Alaska Gyre (Fig. 6-9). The DMS-nitrate relationship may be partially explained
352 by the so-called sulfur overflow hypothesis (Stefels, 2000), which suggests that nutrient-limited phytoplankton
353 increase DMSP production and its subsequent cleavage to DMS, in order to regulate intracellular sulfur quotas
354 when protein synthesis is limited (Hatton & Wilson, 2007; Kinsey et al., 2016; Simó & Vila-Costa, 2006; Spiese
355 & Tatarkov, 2014; Stefels, 2000). This pathway may help explain the higher predicted DMS concentrations
356 predicted at the northern extent of the Alaska Gyre, where SSN concentrations begin to decrease (Fig. 6). The
357 apparent relationship between DMS and nitrate could also result indirectly from the underlying effects of iron
358 limitation. Excess summertime nitrate concentrations are taken as evidence for iron limitation in the NESAP (Boyd
359 and Harrison, 1999; Boyd et al., 2004; Martin and Fitzwater, 1988; Whitney et al., 2005). Under iron-limiting
360 conditions, DMS is thought to function, together with DMSP and DMSO, as part of an antioxidant response to
361 oxidative stress (Sunda et al., 2002). This hypothesis suggests that iron limitation should stimulate net production
362 of DMS and DMSP (Bucciarelli et al., 2013; Sunda et al., 2002), which is inconsistent with the negative dependence
363 predicted between DMS and SSN (Fig. 8b,c).

364   Satellite-based, chlorophyll-normalized fluorescence has been suggested as an additional proxy for iron
365 limitation. Low iron conditions can lead to both a reduction in photosystem I relative to photosystem II (Strzepek
366 and Harrison, 2004), and an apparent increase in energetically-decoupled light harvesting complexes (Allen et al.,
367 2008; Behrenfeld & Milligan, 2013), resulting in elevated fluorescence-to-chlorophyll a ratios (nFLH:Chl-a)
368 (Westberry et al., 2013). To our knowledge, this proxy has not been widely investigated with respect to DMS
369 cycling. In our analysis, we found that nFLH:Chl-a ratios, and the NPQ-corrected fluorescence yields (φ_f), exhibited
370 only weak positive correlations with the RFR and ANN predicted DMS concentrations (Fig. 6, 7). Moreover,
371 neither of these metrics exhibited coherent spatial patterns with predicted DMS concentrations, suggesting a limited
372 role for iron in driving spatial patterns of DMS cycling within the NESAP. However, it is important to note the
373 potential temporal mismatch between our monthly DMS predictions and these more instantaneous metrics of iron
374 limitation, which reflect short-term physiological changes (days to weeks; (Behrenfeld et al., 2009; Westberry et
375 al., 2019) that depend on sporadic iron loading (*e.g.* aerosol deposition; Mahowald et al., 2009). Indeed, both natural

376 and artificial iron-fertilization events have thus far been detected from satellite-derived nFLH:Chl-a at daily

377 resolution (Westberry et al., 2013), in contrast to the monthly-averaged data used here. Therefore, modelling

378 frameworks utilizing shorter temporal scales may find a clearer connection between DMS cycling and iron

379 limitation using the chlorophyll-a fluorescence proxy.

380 Beyond nutrient limitation effects, ambient light fields are believed to exert significant direct and indirect

381 effects on DMS cycling (del Valle et al., 2007). Ultraviolet radiation has been noted to induce high DMS production

382 and turnover through a proposed cascading oxidation pathway, which acts to remove harmful reactive oxygen

383 species (Sunda et al., 2002; Archer et al., 2010). In contrast, more recent evidence has indicated the potential for

384 elevated DMS production in the NESAP from the reduction of DMSO due to light-induced oxidative stress over

385 diurnal cycles (Herr et al., 2020). However, our modelled DMS concentrations exhibited a negative correlation

386 with PAR (Fig. 6, 7), suggesting that incident light may predominantly drive DMS loss in the NESAP through

387 photolysis (del Valle et al., 2007) on regional and longer-term scales.

388 Since DMS does not have strong light absorption properties, the presence of photosensitisers is necessary for

389 the abiotic photooxidation of DMS (Brimblecombe and Shooter, 1986). To account for this process, our models

390 incorporated nitrate (SSN) and a_{cdm}(443) (as a proxy for CDOM; Nelson & Siegel, 2013), both of which are thought

391 to be dominant photosensitisers of DMS in marine systems (Taalba et al., 2013; Bouillon and Miller, 2004, 2005;

392 Galí et al., 2016). In the NESAP, nitrate appears to exert a stronger influence than CDOM on the apparent quantum

393 yields (AQY) of DMS (Bouillon and Miller, 2004). In support of this, our results suggest a stronger negative

394 dependence of predicted DMS concentrations on nitrate compared to CDOM within the NESAP (Fig. 6, 7). We

395 note, however, that the DMS-nitrate relationship likely also reflects physiological impacts of nutrient limitation, as

396 discussed above. Nonetheless, our results are consistent with elevated rates of DMS photo-oxidation in the nitrate-

397 replete, low iron waters of the Alaska Gyre, where photolysis, coupled with potentially high DMS oxidation rates

398 due to iron-induced oxidative stress (Sunda et al., 2002), may explain the low predicted DMS concentrations (Fig.

399 8, 9). Further *in situ* work will be required to resolve the relative contributions of these biotic and abiotic processes

400 to DMS cycling within these areas.

401 Among all the statistical relationships we observed, perhaps the most striking was the association of DMS

402 variability with SSHA, particularly along the Alaskan coast and in relation to mesoscale eddies (Okkonen et al.,

403 2001; Whitney et al., 2005; Fig. 8, 9). To our knowledge, only one other study has linked SSHA to DMS within

404 the NESAP. Herr et al., (2019) demonstrated contrasting positive and negative correlations between DMS and

405 SSHA in offshore and coastal waters, respectively, in general agreement with our results. Presently, the underlying

406 mechanisms explaining the relationship between SSHA and DMS cycling remain unclear, yet it is likely that

407 physical mixing processes are important. For example, enhanced biological production is known to be stimulated
408 by eddy re-supply of iron and macronutrients via vertical advection and diffusion (Whitney et al., 2005; Bailey et
409 al., 2008). These nutrient supply processes would also be expected to influence DMS cycling, as outlined above.
410 Elevated abundances of high DMS-producers within eddies have been noted in the Sargasso Sea (Bailey et al.,
411 2008), while eddy-induced vertical transport likely supplements nearshore, current-driven upwelling that can also
412 resupply iron into the coastal waters of the NESAP (Cullen et al., 2009; Freeland et al., 1984). In addition, eddy
413 propagation can allow cross-shelf transport, distributing micronutrients to offshore waters (Fiechter and Moore,
414 2012), potentially contributing to the apparent elevated DMS concentrations in the outer Alaska gyre between the
415 10.5 and 12°C isotherms (Fig. 8). These mixing and transport mechanisms could partially explain the influence of
416 elevated productivity in driving increased nearshore and northern NESAP DMS concentrations (Fig. 4, 7-9),
417 representing a novel source of DMS variability in this region.

418   The taxonomic composition of plankton assemblages is also a likely source of variability influencing DMS
419 cycling. Significant changes to DMS production and consumption rates within the NESAP are expected in response
420 to variable microbial and phytoplankton taxonomy (Vila-Costa et al., 2006; Lidbury et al., 2016; Sheehan and
421 Petrou, 2020). Such taxonomic variability may, in turn, reflect transient community composition shifts in response
422 to mixing (Bailey et al., 2008), nitrate (Bouillon and Miller, 2004), and iron availability (Levasseur et al., 2006;
423 Merzouk et al., 2006). The monthly averaging used in our data processing removes autocorrelation associated with
424 individual sampling expeditions (Wang et al., 2020), but it may preclude capturing these transient taxonomic
425 responses. For instance, coccolithophores have long been believed to influence DMS cycling in the NESAP (Herr
426 et al., 2019; Asher et al., 2011), yet averaged calcite distributions did not yield increased predictive strength for
427 DMS concentrations in our analysis (see Sect. 2.6). Similarly, applying a chlorophyll-a based taxonomic algorithm
428 (Hirata et al., 2011; Zeng et al., 2018) yielded no further explanation of the DMS variability predicted. The
429 influence of taxonomic composition thus remains cryptic within our modelling framework.

430 **4.2 Implications of Improved Predictive Power**

431   As noted above, both the RFR and ANN approaches demonstrate significantly improved accuracy,
432 explaining up to 62% of observed DMS variability (Fig. 2, 3). This model performance is somewhat lower than
433 that achieved in the prediction of methane fluxes (Weber et al., 2019) and dissolved inorganic carbon dynamics
434 (Roshan and DeVries, 2017), where R^2 values ranging from 0.7 to 0.95 were obtained. Nonetheless, the dramatic
435 accuracy improvement of our algorithms over traditional methods (Fig. 2, 3) encourages the further use of these
436 techniques in modelling DMS distributions.

437   Improved predictive accuracy provides opportunities to gain insight into the mechanisms driving DMS cycling.
438 Our approach has yielded accurate DMS predictions at a 4 to 40-fold higher resolution then previous algorithms
439 (Simó and Dachs, 2002; Vallina and Simó, 2007; Galí et al., 2018; Watanabe et al., 2007), enabling the description
440 of mesoscale patterns and processes (Fig. 8). Extending these methods to sub-mesocale resolution will enable
441 investigations into the dependence of DMS on finer-scale hydrographic processes, particularly stratification and
442 frontal dynamics, which have been increasingly linked to DMS cycling but remain unresolved mechanistically
443 (Asher et al., 2011; Royer et al., 2015). Moreover, coupling machine learning algorithms with biophysical and
444 tracer export models holds promise to resolve the contributions of eddy dynamics and upwelling intensity on DMS
445 variability, likely through nutrient availability and physiological mechanisms (Asher et al., 2011; Bailey et al.,
446 2008; Cullen et al., 2009). Recent work has also developed a new database of DMS apparent quantum yields (Galí
447 et al., 2016). As the availability of these measurements increases, simultaneous mapping of both DMS quantum
448 yields and concentrations will become feasible, enabling future studies to better parse out the contribution of
449 photolysis, physical mixing, and biological drivers of DMS cycling.

450   Although used in a diagnostic capacity here, our statistical models also hold potential for prognostic
451 applications. Frameworks utilizing shorter time scales will likely be able to detect underlying mechanisms
452 driving observed diel cycling (Galí et al., 2013; Royer et al., 2016), even if the underlying mechanisms are still
453 unresolved. We note, however, that caution will need be exercised as machine learning models have a tendency
454 to overfit noise (Weber et al., 2019; Roshan and DeVries, 2017; Wang et al., 2020), thus requiring appropriately
455 large training datasets and the use of known "future" observations to validate predictive accuracy in this context.
456 The significant variability in DMS cycling across oceanic regimes will likely also render predictions more
457 successful at regional, rather than global, scales (Galí et al., 2018; Royer et al., 2015). Nonetheless, prognostic
458 applications of these algorithms should be investigated to aid in the future development of improved mechanistic
459 models.

5 Conclusions

461   We have presented a statistical approach to modelling DMS distributions, which provides significantly
462 higher accuracy than traditional methods (Simó and Dachs, 2002; Vallina and Simó, 2007; Galí et al., 2018;
463 Watanabe et al., 2007; Lana et al., 2011), and yields estimates of the summertime NESAP DMS sea-air fluxes to
464 0.5-2.0 Tg S yr^{-1} in agreement with previous findings (Herr et al., 2019; Lana et al., 2011). Our results further
465 underscore the importance of the NESAP to global DMS production and motivate further observations in

466 traditionally under-sampled areas such as the Alaska Gyre and Aleutian Islands. Although we are unable to directly

467 examine the mechanistic drivers of DMS variability, our findings suggest nutrient limitation, light-driven

468 processes, and eddy-induced mixing are potentially key drivers of DMS cycling in the NESAP. Future studies will

469 benefit from using such statistical algorithms, in conjunction with field-based process studies and mechanistic

470 models, to better understand the underlying dynamics and driving factors in the oceanic DMS cycle.

471 *Code availability.* The analysis in this study makes extensive use of the Numpy, Matplotlib, & Scikit-Learn libraries
472 in Python. The custom codes used can be downloaded at
473 https://github.com/bjmcnabb/DMS_Climatology/tree/main/NESAP or are available upon request from the
474 corresponding author.

475 *Data Availability.* DMS observations and predictor datasets are described in the Methods with relevant links to
476 repositories. Data from the Lana et al. (2011) climatology used for comparison in Table 2 are available via the
477 SOLAs project (retrieved from www.bodc.ac.uk/solas_integration/implementation_products/group1/dms/), where
478 the DMS sea-air fluxes were calculated as described in Sect. 2.3. The gridded climatologies produced from each
479 algorithm in this study can be obtained at
480 https://github.com/bjmcnabb/DMS_Climatology/tree/main/NESAP/Climatologies.

481 *Author Contribution.* BM and PT designed the study. Model code was written and implemented by BM. BM
482 prepared the manuscript with significant contributions from PT.

483 *Competing Interests.* The authors declare that they have no conflict of interest.

484 *Acknowledgements.* We would like to thank Dr. Valentina Radic for her advice in model design. This work was
485 supported by grants to BM and PT from the Natural Sciences and Engineering Research Council of Canada
486 (NSERC).

487

References

488

Allen, A. E., LaRoche, J., Maheswari, U., Lommer, M., Schauer, N., Lopez, P. J., Finazzi, G., Fernie, A. R., and Bowler, C.: Whole-cell response of the pennate diatom Phaeodactylum tricornutum to iron starvation, Proceedings of the National Academy of Sciences, 105, 10438–10443, https://doi.org/10/cs9k8x, 2008.

Archer, S. D., Ragni, M., Webster, R., Airs, R. L., and Geider, R. J.: Dimethyl sulfoniopropionate and dimethyl sulfide production in response to photoinhibition in Emiliania huxleyi, Limnology and Oceanography, 55, 1579–1589, https://doi.org/10/dvpwqb, 2010.

Asher, E. C., Merzouk, A., and Tortell, P. D.: Fine-scale spatial and temporal variability of surface water dimethylsulfide (DMS) concentrations and sea–air fluxes in the NE Subarctic Pacific, Marine Chemistry, 126, 63–75, https://doi.org/10/chmbhk, 2011.

Asher, E. C., Dacey, J. W., Ianson, D., Peña, A., and Tortell, P. D.: Concentrations and cycling of DMS, DMSP, and DMSO in coastal and offshore waters of the Subarctic Pacific during summer, 2010-2011, J. Geophys. Res. Oceans, 122, 3269–3286, https://doi.org/10.1002/2016JC012465, 2017.

Ayers, G. P. and Cainey, J. M.: The CLAW hypothesis: a review of the major developments, Environ. Chem., 4, 366, https://doi.org/10/b7p54b, 2007.

Bailey, K. E., Toole, D. A., Blomquist, B., Najjar, R. G., Huebert, B., Kieber, D. J., Kiene, R. P., Matrai, P., Westby, G. R., and del Valle, D. A.: Dimethylsulfide production in Sargasso Sea eddies, Deep Sea Research Part II: Topical Studies in Oceanography, 55, 1491–1504, https://doi.org/10/fnqb6j, 2008.

Bates, T. S., Lamb, B. K., Guenther, A., Dignon, J., and Stoiber, R. E.: Sulfur emissions to the atmosphere from natural sources, J Atmos Chem, 14, 315–337, https://doi.org/10/chmgt6, 1992.

Behrenfeld, M. J. and Falkowski, P. G.: Photosynthetic rates derived from satellite-based chlorophyll concentration, Limnology and Oceanography, 42, 1–20, https://doi.org/10/cg5x4k, 1997.

Behrenfeld, M. J. and Milligan, A. J.: Photophysiological Expressions of Iron Stress in Phytoplankton, Annu. Rev. Mar. Sci., 5, 217–246, https://doi.org/10.1146/annurev-marine-121211-172356, 2013.

Behrenfeld, M. J., Westberry, T. K., Boss, E. S., O'Malley, R. T., Siegel, D. A., Wiggert, J. D., Franz, B. A., McClain, C. R., Feldman, G. C., Doney, S. C., Moore, J. K., Dall'Olmo, G., Milligan, A. J., Lima, I., and Mahowald, N.: Satellite-detected fluorescence reveals global physiology of ocean phytoplankton, Biogeosciences, 6, 16, https://doi.org/10/fdn3f2, 2009.

Belviso, S., Sciandra, A., and Copin-Montégut, C.: Mesoscale features of surface water DMSP and DMS concentrations in the Atlantic Ocean off Morocco and in the Mediterranean Sea, Deep Sea Research Part I: Oceanographic Research Papers, 50, 543–555, https://doi.org/10.1016/S0967-0637(03)00032-3, 2003.

Bock, J., Michou, M., Nabat, P., Abe, M., Mulcahy, J. P., Olivié, D. J. L., Schwinger, J., Suntharalingam, P., Tjiputra, J., van Hulten, M., Watanabe, M., Yool, A., and Séférian, R.: Evaluation of ocean dimethylsulfide concentration and emission in CMIP6 models, Biogeosciences, 18, 3823–3860, https://doi.org/10/gk6fw8, 2021.

522   Bouillon, R.-C. and Miller, W. L.: Determination of apparent quantum yield spectra of DMS photo-degradation
523   in an in situ iron-induced Northeast Pacific Ocean bloom: AQY of DMS in an iron-induced bloom, Geophys.
524   Res. Lett., 31, n/a-n/a, https://doi.org/10/d96wkn, 2004.

525   Bouillon, R.-C. and Miller, W. L.: Photodegradation of Dimethyl Sulfide (DMS) in Natural Waters: Laboratory
526   Assessment of the Nitrate-Photolysis-Induced DMS Oxidation, Environ. Sci. Technol., 39, 9471–9477,
527   https://doi.org/10/d2j84c, 2005.

528   Boyd, P. and Harrison, P. J.: Phytoplankton dynamics in the NE subarctic Pacific, Deep Sea Research Part II:
529   Topical Studies in Oceanography, 46, 2405–2432, https://doi.org/10/fkg4mz, 1999.

530   Boyd, P. W., Law, C. S., Wong, C. S., Nojiri, Y., Tsuda, A., Levasseur, M., Takeda, S., Rivkin, R., Harrison, P.
531   J., Strzepek, R., Gower, J., McKay, R. M., Abraham, E., Arychuk, M., Barwell-Clarke, J., Crawford, W.,
532   Crawford, D., Hale, M., Harada, K., Johnson, K., Kiyosawa, H., Kudo, I., Marchetti, A., Miller, W., Needoba, J.,
533   Nishioka, J., Ogawa, H., Page, J., Robert, M., Saito, H., Sastri, A., Sherry, N., Soutar, T., Sutherland, N., Taira,
534   Y., Whitney, F., Wong, S.-K. E., and Yoshimura, T.: The decline and fate of an iron-induced subarctic
535   phytoplankton bloom, Nature, 428, 549–553, https://doi.org/10/fkgnf4, 2004.

536   Brimblecombe, P. and Shooter, D.: Photo-oxidation of dimethylsulphide in aqueous solution, Marine Chemistry,
537   19, 343–353, https://doi.org/10/bqwpc9, 1986.

538   Bucciarelli, E., Ridame, C., Sunda, W. G., Dimier-Hugueney, C., Cheize, M., and Belviso, S.: Increased
539   intracellular concentrations of DMSP and DMSO in iron-limited oceanic phytoplankton Thalassiosira oceanica
540   and Trichodesmium erythraeum, Limnology and Oceanography, 58, 1667–1679,
541   https://doi.org/10.4319/lo.2013.58.5.1667, 2013.

542   Charlson, R. J., Lovelock, J. E., Andreae, M. O., and Warren, S. G.: Oceanic phytoplankton, atmospheric
543   sulphur, cloud albedo and climate, Nature, 326, 655–661, https://doi.org/10.1038/326655a0, 1987.

544   Cullen, J. T., Chong, M., and Ianson, D.: British Columbian continental shelf as a source of dissolved iron to the
545   subarctic northeast Pacific Ocean, Global Biogeochem. Cycles, 23, https://doi.org/10/b489x8, 2009.

546   Dacey, J. W. H. and Wakeham, S. G.: Oceanic Dimethylsulfide: Production During Zooplankton Grazing on
547   Phytoplankton, Science, 233, 1314–1316, https://doi.org/10.1126/science.233.4770.1314, 1986.

548   Dickson, D. M. J. and Kirst, G. O.: Osmotic Adjustment in Marine Eukaryotic Algae: The Role of Inorganic Ions,
549   Quaternary Ammonium, Tertiary Sulphonium and Carbohydrate Solutes, New Phytologist, 106, 645–655,
550   https://doi.org/10.1111/j.1469-8137.1987.tb00165.x, 1987.

551   Fiechter, J. and Moore, A. M.: Iron limitation impact on eddy-induced ecosystem variability in the coastal Gulf of
552   Alaska, Journal of Marine Systems, 92, 1–15, https://doi.org/10/bvqv4d, 2012.

553   Franklin, D., Steinke, M., Young, J., Probert, I., and Malin, G.: Dimethylsulphoniopropionate (DMSP), DMSP-
554   lyase activity (DLA) and dimethylsulphide (DMS) in 10 species of coccolithophore, Mar. Ecol. Prog. Ser., 410,
555   13–23, https://doi.org/10/fk7hmj, 2010.

556 Freeland, H. J., Crawford, W. R., and Thomson, R. E.: Currents along the pacific coast of Canada, Atmosphere-
557 Ocean, 22, 151–172, https://doi.org/10.1080/07055900.1984.9649191, 1984.

558 Galí, M., Simó, R., Vila-Costa, M., Ruiz-González, C., Gasol, J. M., and Matrai, P.: Diel patterns of oceanic
559 dimethylsulfide (DMS) cycling: Microbial and physical drivers, Global Biogeochem. Cycles, 27, 620–636,
560 https://doi.org/10.1002/gbc.20047, 2013.

561 Galí, M., Kieber, D. J., Romera-Castillo, C., Kinsey, J. D., Devred, E., Pérez, G. L., Westby, G. R., Marrasé, C.,
562 Babin, M., Levasseur, M., Duarte, C. M., Agustí, S., and Simó, R.: CDOM Sources and Photobleaching Control
563 Quantum Yields for Oceanic DMS Photolysis, Environ. Sci. Technol., 50, 13361–13370,
564 https://doi.org/10/f9jg2w, 2016.

565 Galí, M., Levasseur, M., Devred, E., Simó, R., and Babin, M.: Sea-surface dimethylsulfide (DMS) concentration
566 from satellite data at global and regional scales, Biogeosciences, 15, 3497–3519, https://doi.org/10/gdrm6n, 2018.

567 Garcia, H. E., Weathers, K. W., Paver, C. R., Smolyar, I., Boyer, T. P., Locarnini, M. M., Zweng, M. M.,
568 Mishonov, A. V., Baranova, O. K., and Seidov, D.: World Ocean Atlas 2018. Vol. 4: Dissolved Inorganic
569 Nutrients (phosphate, nitrate and nitrate+ nitrite, silicate), 35pp., 2019.

570 Hatton, A. D. and Wilson, S. T.: Particulate dimethylsulphoxide and dimethylsulphoniopropionate in
571 phytoplankton cultures and Scottish coastal waters, Aquat. Sci., 69, 330–340, https://doi.org/10/dbxk6n, 2007.

572 Hegg, D. A., Radke, L. F., and Hobbs, P. V.: Measurements of Aitken nuclei and cloud condensation nuclei in
573 the marine atmosphere and their relation to the DMS-Cloud-climate hypothesis, J. Geophys. Res. Atmos., 96,
574 18727–18733, https://doi.org/10/d6fwx9, 1991.

575 Herr, A. E., Kiene, R. P., Dacey, J. W. H., and Tortell, P. D.: Patterns and drivers of dimethylsulfide
576 concentration in the northeast subarctic Pacific across multiple spatial and temporal scales, Biogeosciences, 16,
577 1729–1754, https://doi.org/10.5194/bg-16-1729-2019, 2019.

578 Herr, A. E., Dacey, J. W. H., Kiene, R. P., McCulloch, R. D., Schuback, N., and Tortell, P. D.: Potential roles of
579 dimethysulfoxide in regional sulfur cycling and phytoplankton physiological ecology in the NE Subarctic Pacific,
580 Limnology and Oceanography, https://doi.org/10/ghfstm, 2020.

581 Hirata, T., Hardman-Mountford, N. J., Brewin, R. J. W., Aiken, J., Barlow, R., Suzuki, K., Isada, T., Howell, E.,
582 Hashioka, T., Noguchi-Aita, M., and Yamanaka, Y.: Synoptic relationships between surface Chlorophyll-a and
583 diagnostic pigments specific to phytoplankton functional types, Biogeosciences, 8, 311–327,
584 https://doi.org/10.5194/bg-8-311-2011, 2011.

585 Humphries, G. R. W., Deal, C. J., Elliott, S., and Huettmann, F.: Spatial predictions of sea surface
586 dimethylsulfide concentrations in the high arctic, Biogeochemistry, 110, 287–301, https://doi.org/10/fx778z,
587 2012.

588 Kiene, R. P. and Linn, L. J.: The fate of dissolved dimethylsulfoniopropionate (DMSP) in seawater: Tracer
589 studies using 35S-DMSP, Geochimica et Cosmochimica Acta, 64, 2797–2810, https://doi.org/10.1016/S0016-
590 7037(00)00399-9, 2000.

591 Kinsey, J. D., Kieber, D. J., and Neale, P. J.: Effects of iron limitation and UV radiation on Phaeocystis antarctica
592 growth and dimethylsulfoniopropionate, dimethylsulfoxide and acrylate concentrations, Environ. Chem., 13,
593 195–211, https://doi.org/10.1071/EN14275, 2016.

594 Kirst, G. O., Thiel, C., Wolff, H., Nothnagel, J., Wanzek, M., and Ulmke, R.: Dimethylsulfoniopropionate
595 (DMSP) in icealgae and its possible biological role, Marine Chemistry, 35, 381–388,
596 https://doi.org/10.1016/S0304-4203(09)90030-5, 1991.

597 Korhonen, H., Carslaw, K. S., Spracklen, D. V., Mann, G. W., and Woodhouse, M. T.: Influence of oceanic
598 dimethyl sulfide emissions on cloud condensation nuclei concentrations and seasonality over the remote Southern
599 Hemisphere oceans: A global model study, J. Geophys. Res. Atmos., 113, https://doi.org/10/cfrz46, 2008.

600 Lana, A., Bell, T. G., Simó, R., Vallina, S. M., Ballabrera-Poy, J., Kettle, A. J., Dachs, J., Bopp, L., Saltzman, E.
601 S., Stefels, J., Johnson, J. E., and Liss, P. S.: An updated climatology of surface dimethlysulfide concentrations
602 and emission fluxes in the global ocean, Global Biogeochem. Cycles, 25, https://doi.org/10/dbqjrm, 2011.

603 Levasseur, M., Scarratt, M. G., Michaud, S., Merzouk, A., Wong, C. S., Arychuk, M., Richardson, W., Rivkin, R.
604 B., Hale, M., Wong, E., Marchetti, A., and Kiyosawa, H.: DMSP and DMS dynamics during a mesoscale iron
605 fertilization experiment in the Northeast Pacific-Part I: Temporal and vertical distributions, Deep Sea Research
606 Part II: Topical Studies in Oceanography, 53, 2353–2369, https://doi.org/10.1016/j.dsr2.2006.05.023, 2006.

607 Li, Z. and Cassar, N.: Satellite estimates of net community production based on O_2/Ar observations and
608 comparison to other estimates, Global Biogeochem. Cycles, 30, 735–752, https://doi.org/10/f8v6bh, 2016.

609 Lidbury, I., Kröber, E., Zhang, Z., Zhu, Y., Murrell, J. C., Chen, Y., and Schäfer, H.: A mechanism for bacterial
610 transformation of dimethylsulfide to dimethylsulfoxide: a missing link in the marine organic sulfur cycle,
611 Enviorn. Microbiol., 18, 2754–2766, https://doi.org/10.1111/1462-2920.13354, 2016.

612 Livingstone, D. M. and Imboden, D. M.: The non-linear influence of wind-speed variability on gas transfer in
613 lakes, Tellus B, 45, 275–295, https://doi.org/10/bbc4n3, 1993.

614 Mahowald, N. M., Engelstaedter, S., Luo, C., Sealy, A., Artaxo, P., Benitez-Nelson, C., Bonnet, S., Chen, Y.,
615 Chuang, P. Y., Cohen, D. D., Dulac, F., Herut, B., Johansen, A. M., Kubilay, N., Losno, R., Maenhaut, W.,
616 Paytan, A., Prospero, J. M., Shank, L. M., and Siefert, R. L.: Atmospheric Iron Deposition: Global Distribution,
617 Variability, and Human Perturbations, Annu. Rev. Mar. Sci., 1, 245–278, https://doi.org/10/fsn8tj, 2009.

618 Malin, G., Wilson, W. H., Bratbak, G., Liss, P. S., and Mann, N. H.: Elevated production of dimethylsulfide
619 resulting from viral infection of cultures of Phaeocystis pouchetii, Limnology and Oceanography, 43, 1389–1393,
620 https://doi.org/10/bw7vjf, 1998.

621 Martin, J. H. and Fitzwater, S. E.: Iron deficiency limits phytoplankton growth in the north-east Pacific subarctic,
622 Nature, 331, 341–343, https://doi.org/10/bvtg6v, 1988.

623 Merzouk, A., Levasseur, M., Scarratt, M. G., Michaud, S., Rivkin, R. B., Hale, M. S., Kiene, R. P., Price, N. M.,
624 and Li, W. K. W.: DMSP and DMS dynamics during a mesoscale iron fertilization experiment in the Northeast
625 Pacific-Part II: Biological cycling, 53, 2370–2383, https://doi.org/10.1016/j.dsr2.2006.05.022, 2006.

626 Nelson, N. B. and Siegel, D. A.: The Global Distribution and Dynamics of Chromophoric Dissolved Organic
627 Matter, Annu. Rev. Mar. Sci., 5, 447–476, https://doi.org/10/dcwcbk, 2013.

628 Nemcek, N., Ianson, D., and Tortell, P. D.: A high-resolution survey of DMS, CO2, and O2/Ar distributions in
629 productive coastal waters, Global Biogeochem. Cycles, 22, 1–13, https://doi.org/10.1029/2006gb002879, 2008.

630 Nevitt, G. A.: Sensory ecology on the high seas: the odor world of the procellariiform seabirds, Journal of
631 Experimental Biology, 211, 1706–1713, https://doi.org/10/d2rdz3, 2008.

632 Nightingale, P. D., Malin, G., Law, C. S., Watson, A. J., Liss, P. S., Liddicoat, M. I., Boutin, J., and Upstill-
633 Goddard, R. C.: In situ evaluation of air-sea gas exchange parameterizations using novel conservative and
634 volatile tracers, Global Biogeochem. Cycles, 14, 373–387, https://doi.org/10/d9dztz, 2000.

635 Okkonen, S. R., Jacobs, G. A., Joseph Metzger, E., Hurlburt, H. E., and Shriver, J. F.: Mesoscale variability in
636 the boundary currents of the Alaska Gyre, Continental Shelf Research, 21, 1219–1236, https://doi.org/10/dc2n79,
637 2001.

638 Roshan, S. and DeVries, T.: Efficient dissolved organic carbon production and export in the oligotrophic ocean,
639 Nat Commun, 8, 2036, https://doi.org/10/gcrfdg, 2017.

640 Royer, S.-J., Galí Tàpias, M., Saltzman, E., Mccormick, C., Bell, T., and Simó, R.: Development and validation
641 of a shipboard system for measuring high-resolution vertical profiles of aqueous dimethylsulfide concentrations
642 using chemical ionisation mass spectrometry, Environmental Chemistry, https://doi.org/10/f6c3qp, 2014.

643 Royer, S.-J., Mahajan, A. S., Galí, M., Saltzman, E., and Simó, R.: Small-scale variability patterns of DMS and
644 phytoplankton in surface waters of the tropical and subtropical Atlantic, Indian, and Pacific Oceans, Geophys.
645 Res. Lett., 42, 475–483, https://doi.org/10/gkxzf6, 2015.

646 Royer, S.-J., Galí, M., Mahajan, A. S., Ross, O. N., Pérez, G. L., Saltzman, E. S., and Simó, R.: A high-resolution
647 time-depth view of dimethylsulphide cycling in the surface sea, Sci. Rep., 6, 32325,
648 https://doi.org/10.1038/srep32325, 2016.

649 Saltzman, E. S., King, D. B., Holmen, K., and Leck, C.: Experimental determination of the diffusion coefficient
650 of dimethylsulfide in water, J. Geophys. Res. Oceans, 98, 16481–16486, https://doi.org/10/c73n5b, 1993.

651 Saltzman, E. S., Bruyn, W. J. D., Lawler, M. J., Marandino, C. A., and McCormick, C. A.: A chemical ionization
652 mass spectrometer for continuous underway shipboard analysis of dimethylsulfide in near-surface seawater,
653 Ocean Sci., 10, https://doi.org/10/bv59ng, 2009.

654 Schmidtko, S., Johnson, G. C., and Lyman, J. M.: MIMOC: A global monthly isopycnal upper-ocean climatology
655 with mixed layers, J. Geophys. Res. Oceans, 118, 1658–1672, https://doi.org/10/ggqp4h, 2013.

656 Sheehan, C. E. and Petrou, K.: Dimethylated sulfur production in batch cultures of Southern Ocean
657 phytoplankton, Biogeochemistry, 147, 53–69, https://doi.org/10/ghjqgm, 2020.

658 Simó, R. and Dachs, J.: Global ocean emission of dimethylsulfide predicted from biogeophysical data, Global
659 Biogeochem. Cycles, 16, 26-1-26–10, https://doi.org/10/cmqkh2, 2002.

660 Simó, R. and Vila-Costa, M.: Ubiquity of algal dimethylsulfoxide in the surface ocean: Geographic and temporal
661 distribution patterns, Marine Chemistry, 100, 136–146, https://doi.org/10/bg5bph, 2006.

662 Spiese, C. and Tatarkov, E.: Dimethylsulfoxide reduction activity is linked to nutrient stress in Thalassiosira
663 pseudonana NCMA 1335, Mar. Ecol. Prog. Ser., 507, 31–38, https://doi.org/10.3354/meps10842, 2014.

664 Spiese, C. E., Kieber, D. J., Nomura, C. T., and Kiene, R. P.: Reduction of dimethylsulfoxide to dimethylsulfide
665 by marine phytoplankton, Limnology and Oceanography, 54, 560–570,
666 https://doi.org/10.4319/lo.2009.54.2.0560, 2009.

667 Stefels, J.: Physiological aspects of the production and conversion of DMSP in marine algae and higher plants,
668 Journal of Sea Research, 43, 183–197, https://doi.org/10.1016/S1385-1101(00)00030-7, 2000.

669 Strzepek, R. F. and Harrison, P. J.: Photosynthetic architecture differs in coastal and oceanic diatoms, Nature,
670 431, 689–692, https://doi.org/10/fk2fs7, 2004.

671 Sunda, W. G., Kieber, D., and Kiene, R. P.: An antioxidant function of DMSP and DMS in marine algae Oceanic
672 dimethylsulfide (DMS) photolysis, Nature, 418, 317–320, https://doi.org/10.1038/nature00851, 2002.

673 Taalba, A., Xie, H., Scarratt, M. G., Bélanger, S., and Levasseur, M.: Photooxidation of dimethylsulfide (DMS)
674 in the Canadian Arctic, Biogeosciences, 10, 6793–6806, https://doi.org/10/f5jhsv, 2013.

675 Tortell, P. D.: Dissolved gas measurements in oceanic waters made by membrane inlet mass spectrometry,
676 Limnology and Oceanography: Methods, 3, 24–37, https://doi.org/10/drmjv5, 2005a.

677 Tortell, P. D.: Small-scale heterogeneity of dissolved gas concentrations in marine continental shelf waters,
678 Geochemistry, Geophysics, Geosystems, 6, https://doi.org/10/bgqvs9, 2005b.

679 del Valle, D. A., Kieber, D. J., Bisgrove, J., and Kiene, R. P.: Light-Stimulated Production of Dissolved DMSO
680 by a Particle-Associated Process in the Ross Sea, Antarctica, Limnology and Oceanography, 52, 2456–2466,
681 https://doi.org/10.4319/lo.2007.52.6.2456, 2007.

682 Vallina, S. M. and Simó, R.: Strong relationship between DMS and the solar radiation dose over the global
683 surface ocean, Science, 315, 506–508, https://doi.org/10.1126/science.1133680, 2007.

684 Vila-Costa, M., Valle, D. A. D., González, J. M., Slezak, D., Kiene, R. P., Sánchez, O., and Simó, R.:
685 Phylogenetic identification and metabolism of marine dimethylsulfide-consuming bacteria, 8, 2189–2200,
686 https://doi.org/10.1111/j.1462-2920.2006.01102.x, 2006.

687 Wang, W.-L., Song, G., Primeau, F., Saltzman, E. S., Bell, T. G., and Moore, J. K.: Global ocean dimethyl
688 sulfide climatology estimated from observations and an artificial neural network, Biogeosciences, 17, 5335–5354,
689 https://doi.org/10/ghn33p, 2020.

690   Watanabe, Y. W., Yoshinari, H., Sakamoto, A., Nakano, Y., Kasamatsu, N., Midorikawa, T., and Ono, T.:
691   Reconstruction of sea surface dimethylsulfide in the North Pacific during 1970s to 2000s, Marine Chemistry,
692   103, 347–358, https://doi.org/10/bzz33z, 2007.

693   Webb, A. L., van Leeuwe, M. A., den Os, D., Meredith, M. P., J. Venables, H., and Stefels, J.: Extreme spikes in
694   DMS flux double estimates of biogenic sulfur export from the Antarctic coastal zone to the atmosphere, Sci.
695   Rep., 9, 2233, https://doi.org/10/ghjqgc, 2019.

696   Weber, T., Wiseman, N. A., and Kock, A.: Global ocean methane emissions dominated by shallow coastal
697   waters, Nat. Commun., 10, 4584, https://doi.org/10/gf9pc7, 2019.

698   Westberry, T. K., Behrenfeld, M. J., Milligan, A. J., and Doney, S. C.: Retrospective satellite ocean color analysis
699   of purposeful and natural ocean iron fertilization, Deep Sea Research Part I: Oceanographic Research Papers, 73,
700   1–16, https://doi.org/10/f4rcbn, 2013.

701   Westberry, T. K., Shi, Y. R., Yu, H., Behrenfeld, M. J., and Remer, L. A.: Satellite-Detected Ocean Ecosystem
702   Response to Volcanic Eruptions in the Subarctic Northeast Pacific Ocean, Geophys. Res. Lett., 46, 11270–11280,
703   https://doi.org/10/ggr9ms, 2019.

704   Whitney, F. A., Crawford, W. R., and Harrison, P. J.: Physical processes that enhance nutrient transport and
705   primary productivity in the coastal and open ocean of the subarctic NE Pacific, Deep Sea Research Part II:
706   Topical Studies in Oceanography, 52, 681–706, https://doi.org/10/dkn9sn, 2005.

707   Zeng, C., Rosengard, S. Z., Burt, W., Peña, M. A., Nemcek, N., Zeng, T., Arrigo, K. R., and Tortell, P. D.:
708   Optically-derived estimates of phytoplankton size class and taxonomic group biomass in the Eastern Subarctic
709   Pacific Ocean, Deep Sea Research Part I: Oceanographic Research Papers, 136, 107–118,
710   https://doi.org/10.1016/j.dsr.2018.04.001, 2018.

711